Contents lists available at ScienceDirect

Nuclear Instruments and Methods in Physics Research A

journal homepage: www.elsevier.com/locate/nima

MINERvA neutrino detector response measured with test beam data

L. Aliaga [a,1], O. Altinok [c], C. Araujo Del Castillo [b], L. Bagby [d], L. Bellantoni [d], W.F. Bergan [a],
A. Bodek [e], R. Bradford [e,1], A. Bravar [f], H. Budd [e], A. Butkevich [g], D.A. Martinez Caicedo [h,d],
M.F. Carneiro [h], M.E. Christy [i], J. Chvojka [e], H. da Motta [h], J. Devan [a], G.A. Díaz [e,b],
S.A. Dytman [j], B. Eberly [j,2], J. Felix [k], L. Fields [l], R. Fine [e], R. Flight [e], A.M. Gago [b], C. Gingu [d],
T. Golan [e,d], A. Gomez [e], R. Gran [m,*], D.A. Harris [d], A. Higuera [e,k,3], I.J. Howley [a], K. Hurtado [h,n],
J. Kleykamp [e], M. Kordosky [a], M. Lanari [m], T. Le [o], A.J. Leister [a], A. Lovlein [m], E. Maher [p],
W.A. Mann [c], C.M. Marshall [e], K.S. McFarland [e,d], C.L. McGivern [j], A.M. McGowan [e],
B. Messerly [j], J. Miller [q], W. Miller [m], A. Mislivec [e], J.G. Morfín [d], J. Mousseau [r], T. Muhlbeier [h],
D. Naples [j], J.K. Nelson [a], A. Norrick [a], N. Ochoa [b], C.D. O'Connor [a], B. Osmanov [r], J. Osta [d],
V. Paolone [j], C.E. Patrick [l], L. Patrick [l], G.N. Perdue [d,e], C.E. Pérez Lara [b],
L. Rakotondravohitra [d,4], H. Ray [r], L. Ren [j], P.A. Rodrigues [e], P. Rubinov [d], C.R. Rude [m],
D. Ruterbories [e], H. Schellman [l], D.W. Schmitz [d], C.J. Solano Salinas [n], N. Tagg [s], B.G. Tice [o,1],
Z. Urrutia [k], E. Valencia [k], T. Walton [i,5], A. Westerberg [m], J. Wolcott [e], N. Woodward [m],
M. Wospakrik [r], G. Zavala [k], D. Zhang [a], B.P. Ziemer [t]

[a] Department of Physics, College of William & Mary, Williamsburg, VA 23187, USA
[b] Sección Física, Departamento de Ciencias, Pontificia Universidad Católica del Perú, Apartado 1761, Lima, Peru
[c] Physics Department, Tufts University, Medford, MA 02155, USA
[d] Fermi National Accelerator Laboratory, Batavia, IL 60510, USA
[e] University of Rochester, Rochester, New York 14627, USA
[f] University of Geneva, 1211 Geneva 4, Switzerland
[g] Institute for Nuclear Research of the Russian Academy of Sciences, 117312 Moscow, Russia
[h] Centro Brasileiro de Pesquisas Físicas, Rua Dr. Xavier Sigaud 150, Urca, Rio de Janeiro, Rio de Janeiro 22290-180, Brazil
[i] Hampton University, Department of Physics, Hampton, VA 23668, USA
[j] Department of Physics and Astronomy, University of Pittsburgh, Pittsburgh, PA 15260, USA
[k] Campus León y Campus Guanajuato, Universidad de Guanajuato, Lascurain de Retana No. 5, Colonia Centro, Guanajuato 36000, Guanajuato, Mexico
[l] Northwestern University, Evanston, IL 60208, USA
[m] Department of Physics, University of Minnesota – Duluth, Duluth, Minnesota 55812, USA
[n] Universidad Nacional de Ingeniería, Apartado 31139, Lima, Peru
[o] Rutgers, The State University of New Jersey, Piscataway, NJ 08854, USA
[p] Massachusetts College of Liberal Arts, 375 Church Street, North Adams, MA 01247, USA
[q] Departamento de Física, Universidad Técnica Federico Santa María, Avenida España 1680 Casilla 110-V, Valparaíso, Chile
[r] University of Florida, Department of Physics, Gainesville, FL 32611, USA
[s] Department of Physics, Otterbein University, 1 South Grove Street, Westerville, OH 43081, USA
[t] Department of Physics and Astronomy, University of California, Irvine, Irvine, CA 92697-4575, USA

ARTICLE INFO

ABSTRACT

The MINERvA collaboration operated a scaled-down replica of the solid scintillator tracking and sampling calorimeter regions of the MINERvA detector in a hadron test beam at the Fermilab Test Beam Facility. This paper reports measurements with samples of protons, pions, and electrons from 0.35 to 2.0 GeV/c momentum. The calorimetric response to protons, pions, and electrons is obtained from these data. A measurement of the parameter in Birks' law and an estimate of the tracking efficiency are extracted from

* Corresponding author.
  [1] Now at Argonne National Laboratory, Argonne, IL 60439, USA.
  [2] Now at SLAC National Accelerator Laboratory, Stanford, CA 94309, USA.
  [3] University of Houston, Houston, TX 77204, USA.
  [4] Also at Department of Physics, University of Antananarivo, Madagascar.
  [5] Now at Fermi National Accelerator Laboratory, Batavia, IL 60510, USA.

the proton sample. Overall the data are well described by a Geant4-based Monte Carlo simulation of the detector and particle interactions with agreements better than 4% for the calorimetric response, though some features of the data are not precisely modeled. These measurements are used to tune the MINERvA detector simulation and evaluate systematic uncertainties in support of the MINERvA neutrino cross-section measurement program.

1. Introduction and test beam goals

The MINERvA experiment [1] is designed to make precision measurements of neutrino-nucleus cross-sections. An important part of these [2–6] and future cross-section measurements is the estimate of the energy of one or more hadrons exiting the nucleus. These hadrons include recoil protons and neutrons with kinetic energies from hundreds of MeV to a few GeV, pions from inelastic production, and softer nucleons and nuclear fragments. The goal of the test beam experiment is to measure how well the Monte Carlo (MC) simulation of the detector response of these particles describes the data. The accuracy of the simulated single-particle response is an essential ingredient to the MINERvA neutrino cross-section measurements. Results presented in this paper include a measurement of Birks' law parameter [7,8], constraints on the accuracy of proton, pion, and electron calorimetry, and study of tracking efficiency for protons.

The detector used to take these data is a miniature replica of MINERvA. It is 1 m in the transverse dimension, about half the size as MINERvA, and one-third the depth. These test beam data are the first from a new hadron beamline at the Fermilab Test Beam Facility (FTBF) built for a data run in summer 2010 as Fermilab Test Beam Experiment T977. There are differences between the two detectors that mitigate special aspects of the beam environment in FTBF. They include every-other-side readout and higher light yield per MeV, and allow for a data set better suited for Birks' parameter and calorimetry measurements.

The energy range covered by these data, 0.35–2.0 GeV, is well matched to the energy range of protons, pions, and electromagnetic showers in the 2010–2012 MINERvA low-energy neutrino and antineutrino data. This is especially true for the reactions from neutrino quasielastic scattering through Δ and N* resonance production. Measuring differential cross-sections for these exclusive final states is a pillar of the MINERvA neutrino physics program. These energies also cover the lower part of the range expected for hadrons produced in neutrino deep inelastic scattering.

This paper starts with a description of the test beam and associated instrumentation, then the detector, followed by the resulting data sample with its simulation and calibrations. Birks' law parameter measurement is the next because the parameter is used for all other analyses. Proton calorimetry results are presented followed by a section with a complete discussion of systematic uncertainties for proton, pion, and electron measurements, which share the same sources but take on different values. With the uncertainty discussion as a prelude, the pion calorimetry results are described, followed by the electron calorimetry results, and then a discussion of calorimetry with respect to other experimental results. The paper concludes with a measurement of tracking efficiency and a summary.

2. Fermilab Test Beam Facility tertiary hadron beam

This beam was developed through a partnership between the MINERvA experiment and the Fermilab Test Beam Facility. It is produced from 16 GeV pions colliding with a copper target. All species exit a collimator with an angle of $16 \pm 1°$ from the direction of the incident pions. The species and momentum are tagged particle-by-particle using time-of-flight (TOF) and position measurements from four wire chambers. Fig. 1 shows the geometry and coordinate system viewed from the top with the beam propagating left to right. The incident 16 GeV pions initially encounter the target and collimator, and the products of interactions in the target continue toward two magnets. The magnets are type "NDB" made at Fermilab, are ramped to a current of 100 A producing a 0.339 Tesla field in the central region of the magnet, and have a polarity that can be reversed. The typical field integral is 38.3 Tesla cm with 1.5 Tesla cm variations around this value that encompass 90% of selected events. The detector, which is on the right, sees a range of incident particles with low momentum at low horizontal (Y) coordinate and normal incidence, with high momentum at higher Y-coordinates and angles as far as 10° from the detector axis. In addition to the correlation, the wide apertures cause an intrinsic dispersion such that particles of the same momentum reach the detector spread over a tens of centimeters horizontally. The dispersion also ensures that particles of the same momentum are being measured by a range of physical scintillator strips in each plane.

The four wire chambers were originally built for the HyperCP experiment [9] in the late 1990s. The upstream two have an aperture of 457×254 mm with a wire pitch of 1.016 mm in X, U, X′, V configuration with U and V rotated by $\pm 26.57°$. The downstream two are larger, with an aperture of 559×305 mm and wire pitch 1.270 mm. The planes and original electronics were refurbished for our use.
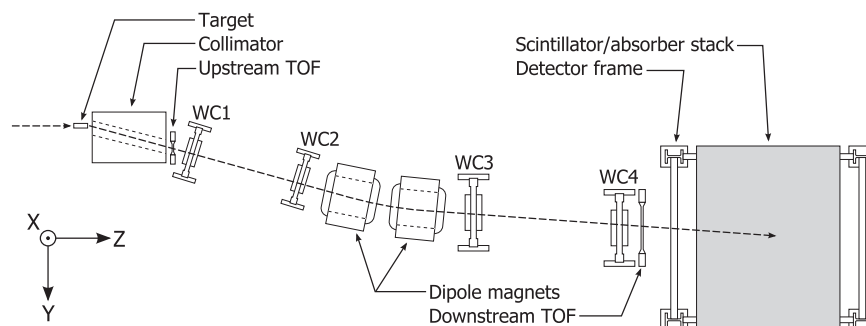

Fig. 1. Diagram of the beamline built for this experiment, viewed from above with the beam going from left to right.

The TOF units are used to measure the time the particle travels from just in front of the first wire chamber to just behind the last wire chamber. The path length is 6.075 m with RMS variations of 0.014 m from center to inside and outside tracks through the bend magnets. The front TOF unit is a single piece of inch-thick scintillator. The back unit is three longer pieces of inch-thick scintillator, covering an area larger than the wire chamber aperture. A resolution of 200 ps is obtained using fast photo-multiplier tubes (PMTs) reading out two sides of each scintillator and a 25 ps least-count time to digital converter. The photo-electron yield, scintillator size, and length of signal cables contribute to this resolution.

With the 1.07 m wide detector, large magnet and wire chamber apertures, and our chosen beam tune, the beam delivers a broad distribution of protons and pions from 0.35 to 3.0 GeV/c in momentum. The usable momentum range for these analyses is 0.35–2.0 GeV/c which provides proton, π^+, and π^- samples, each total roughly 10 000 particles. The electron content of the beam is small and limited to momenta below 0.5 GeV/c, but has enough events that statistical uncertainties are smaller than systematic uncertainties. In addition, there is a 5% kaon component, plus smaller components of deuterons and alpha particles which are not included in the results presented here.

The pion, kaon, proton, and deuteron/alpha components are well separated, shown in Fig. 2 after quality cuts to ensure only well-reconstructed particles. Low momentum electrons are barely discernable near 20 ns in this figure. There is also an accidental background near 39 ns when another particle coincidentally passes early through the upstream TOF. These protons and pions happen because the Fermilab Main Injector Accelerator supplying the beam has a 53 MHz time structure. Another pion striking the copper target earlier than the triggered proton, kaon, or pion particle can produce a particle that passes through the upstream TOF, creating a timing artifact at integer multiples of 19 ns.

The separation shown in Fig. 2 allows species to be selected based on momentum, TOF, or the combination of the two plus the measured path length that gives an estimator for the mass of the particle. Protons (and kaons) are selected by requiring the estimated mass be within $\pm 20\%$ of the true mass of the particle. The selection is wider for pions and based on TOF because the TOF resolution is the limiting factor and we do not cut events if their TOF measurement fluctuates to superluminal. The lower bound is the expected TOF of a pion less 0.5 ns and rejects electrons; the upper end is based on the TOF for the pion mass plus 20% plus an extra 0.5 ns. An additional cut from 38 to 41 ns rejects the accidental pion background in the proton sample. The purities of the pion and proton selection are better than 99%, as estimated by extrapolating the tails of the wrong-species distribution under the selected events, plus additional ab initio simulation of the electron content of the beamline design. The

electron selection is more complex and includes pion rejection criteria, as described in Section 9.

The momentum estimate is accurate to 1% at low energy and 2% at high energy. It uses a detailed map of the magnetic field calculated using finite element analysis software from the specifications for the two dipole magnet coils and steel and the position survey of their placement relative to each other. The central value of the magnetic field from the calculation is adjusted down 0.58% to match the actual field of the magnet from in situ measurements. Measurements of the field were taken by stepping a 3D Hall probe through the magnet along vertical, longitudinal, and transverse lines with both magnets installed in their final positions. The field measurements are well described by the calculated field. The description of the principle component of the field along an axis through the magnets, especially the longitude extent of the field, is the most important feature constrained by the measurements and contributes a 0.5% uncertainty in the momentum. The other uncertainty comes from the accuracy of the position survey of the four wire chambers.

The momentum resolution is also evaluated particle-by-particle. It is 2.5% for pions and ranges monotonically from 5% to 3% for low to high momentum protons. It is driven by multiple scattering and nonuniform magnetic field effects at low momenta and by the wire pitch and beamline length at high momenta. The iterative momentum fit steps along a candidate trajectory through the nonuniform calculated field to estimate the field integral. Then a Kalman filter technique [10] is used to obtain the momentum and its uncertainty for each particle. The resolution of the momentum estimate is modeled accurately enough and is not a limiting factor for these analyses.

3. MINERvA test beam detector and calibration

The detector exposed to this FTBF beam (hereafter called the test beam detector) is a miniature version of the MINERvA detector installed in the NuMI neutrino beam [1] (hereafter called the MINERvA detector). It is made of 40 square planes of 63 nested, triangle-shaped scintillator strips each with length 107 cm and thickness 1.7 cm. This contrasts with the MINERvA detector which has a hexagonal cross-section and is made of 124 planes of 127 strips in the central tracker region followed by another 20 planes each of electromagnetic calorimeter (ECAL) and hadron calorimeter (HCAL) which have lead and iron interleaved respectively. Both detectors share the same three-view UXVX sequence of planes with U and V rotated $\pm 60^\circ$ relative to the X plane that defines (for the test beam detector) the vertical coordinate system. Three views allow for reconstruction of multiple tracks for the MINERvA detector and very good reconstruction of single tracks in the test beam detector.

Unlike the MINERvA detector, the test beam detector's removable absorber planes allow us to take exposures in two configurations. One has 20 planes with 1.99 mm thick lead absorber (ECAL) followed by 20 planes with 26.0 mm thick iron absorber (HCAL). The absorber is interleaved by placing one absorber upstream of each scintillator plane. The other has 20 planes with no absorber (tracker) followed by 20 planes of ECAL. For compactness, this paper will refer to these configurations as EH and TE, respectively.

As illustrated in the left panel of Fig. 3, the first nine planes of the TE are shown with no absorber. Starting before the 20th plane, another hanger with a sheet of lead would be lowered before each succeeding scintillator plane. For the EH configuration, a hanger holding a lead sheet is installed before the first U plane and for all the first 20 planes. Then a hanger with an iron plate is installed in front of each of the remaining 20 planes. The right panels are modified from the web-based event displays [11] for two events from data.
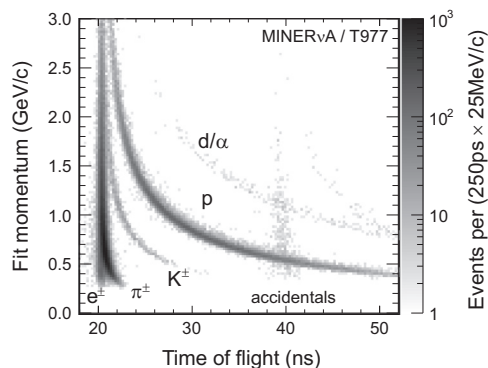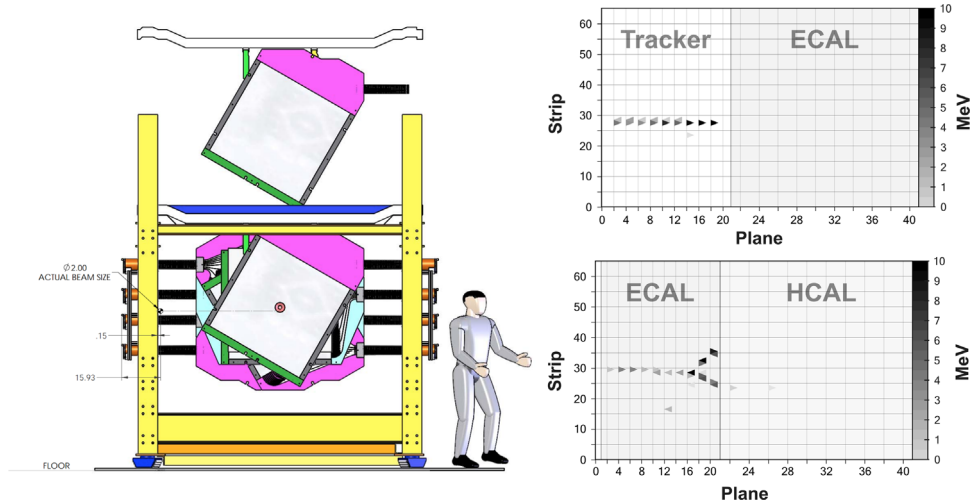

Fig. 2. The measured momentum and time-of-flight used to separate different particle species and backgrounds. The origin of the backgrounds from the accelerator timing structure are described in the text.

Fig. 3. A drawing of the detector viewed from the front (left). The third U plane is being lowered onto the stand behind eight installed planes. The drawing also illustrates the every other side readout in sets of four. If this was the ECAL, there would be a plane of lead absorber between each plane. A proton (right top) stopping at the end of its range in plane 18 of the TE configuration and a pion (right bottom) interacting near plane 16 of the EH configuration. The aspect ratios for the right plots are not to scale and only activity in the X vew planes are shown.

They show side view of the X planes for a proton in the TE and a pion in the EH detector configurations. The design replicates the main downstream region of the MINERvA detector, which has 124 planes of tracker followed by 20 planes of ECAL and 20 planes of HCAL.

The readout chain from scintillator to wavelength-shifting (WLS) fiber to photomultiplier tube (PMT) [1] to digitization [12] is almost identical between the test beam and the MINERvA detectors. The exception is that the test beam detector has no clear fiber optical cables; the WLS fiber connects directly to the PMT a half-meter out of the plane. The effect of smaller scintillator planes and no clear fiber is that the test beam detector has about 50% higher light yield for a given energy deposit, and correspondingly better resolution for some kinds of measurements compared to the MINERvA detector. The Hamamatsu H8804MOD-2 multi-anode PMTs are the same. The front end electronics and DAQ [12] save the same 16 μs of data in response to the trigger, and are only modified to operate in response to a trigger formed by beamline instrumentation or cosmic ray trigger scintillator rather than the predictable arrival of a trigger from the NuMI beamline.

Unlike the MINERvA detector, in which the PMT assemblies for every plane are on the same side, on the test beam detector, the assemblies are alternated in groups of four planes, one UXVX set rotated 180°. Mechanically this allows the planes to be placed closer together than the frames and PMT assemblies would otherwise permit. The result is an air-filled space only slightly larger than in the MINERvA detector. Because the beam bend-magnets steer different momentum particles to different portions of the detector (and at different angles), there is a correlation between the geometry and the position-dependent optical attenuation of the readout. Alternating the readout mitigates a few-percent momentum dependent uncertainty, making this effect negligible.

The detector energy scale is calibrated using the same strategy described in [1] for the MINERvA detector. An initial estimate for photoelectron yield is obtained for each strip using pedestal subtraction and a gain measurement based on the light injection system. The intrinsic differences in response between strips are analyzed using through-going muons to produce a correction factor to make the average response uniform from strip to strip. As a side effect, these muons give geometric plane position corrections.

The absolute energy scale is determined using a muon equivalent unit technique. The peak number of photoelectrons at the PMT is tuned to be the same in the data and simulation, and the simulated geometry and Geant4 energy loss are used to set the absolute energy scale. The calibration uses the peak of the ΔE/plane response for muons, and depends little on muon δ-ray and bremsstrahlung production in the tail of that distribution. One difference between the test beam detector and the MINERvA detector calibrations is that the former uses broad spectrum cosmic ray muons, and a simulated spectrum with the same angular distribution, rather than momentum-analyzed muons from the NuMI beam. As with the MINERvA detector, these calibrations do not include energy that appears off the muon track due to crosstalk, a feature treated separately in the analyses described in this paper.

Temperature dependence is more important for the test beam detector than it is in the NuMI hall. Hadron beam data were taken in June and July 2010, usually during the hours from 04:00 to 18:00. In addition to day–night thermal changes, the heat load from operating the magnets and wire chamber electronics warmed the experimental hall during the day, which then cooled at night. Thus, the overnight cosmic muon sample spans the same 23–34 °C range of temperature as the daytime hadron sample. The detector response is corrected for the measured temperature dependence on a plane-by-plane basis and a residual uncertainty is included with the systematic uncertainties. Each plane is connected to a single PMT, but the temperature dependence is the sum of effects due to the scintillator, WLS fiber, and PMT. Averaged over all planes, the effect on the energy scale is $-0.42 \pm 0.04\%$/C for the EH configuration and $-0.37 \pm 0.03\%$/C for the TE configuration.

4. Data sample and simulation

The incident particle momentum spectra for the selected data samples and the matching simulated spectra are shown in Fig. 4. There are plots of the energy spectra for protons in the TE configuration and p, π^+, and π^- in the EH configuration. At these momenta, pions leave the back of the TE detector and are not used for a calorimetric analysis. The data samples are selected using the momentum and time-of-flight measurements shown in Fig. 2 and discussed in Section 2. The proton distribution is not smooth at 0.15 GeV because of the extra TOF-based pion-background rejection.

In this analysis, the data are compared to a detailed, high-statistics Monte Carlo simulation (MC). The different species' spectra for the simulation are generated from the *data* particles' position and momentum measured at the third wire chamber, with momentum and angle smeared according to the estimated
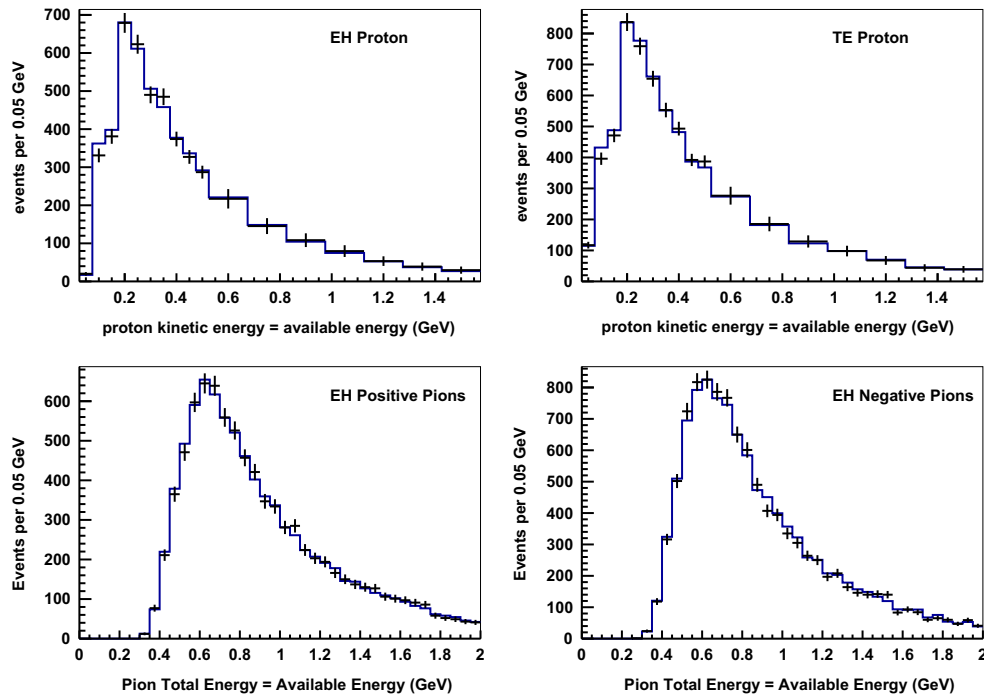
Fig. 4. Measured spectra for EH proton (top left), TE proton (top right), EH π^+ (bottom left), EH π^- (bottom right) samples, after selection. The histogram is taken from a Monte Carlo simulation that was seeded with measured particle momenta and trajectories from the data, so by construction the spectra are the same.

Table 1
Summary of the as-simulated material composition for each detector region. The nuclear interaction length and the radiation length are for twenty planes, the others are per-plane.

Subdetector	Material (g/cm^2)	Percent uncertainty	Air gap (mm)	Interaction lengths	Radiation lengths
Tracker	2.027	1.5%	2.2	0.5	0.9
ECAL	2.30 + 2.027	1.2% + 1.5%	8.1	0.7	8
HCAL	20.4 + 2.027	1.2% + 1.5%	3.5	3.6	30

resolution on a particle-by-particle basis. The simulation then propagates particles through the material of the third and fourth wire chamber, the downstream TOF, the cosmic muon trigger scintillator, the air, and finally into the test beam detector. Using the estimated energy and position resolution for each particle, we apply a Gaussian random smearing and use the same initial particle position and momentum multiple times. The resulting MC samples are typically 20–40 times larger than the data, depending on the analysis. In our limit of excellent resolution, this method is adequate to replace a full unfolding of the resolution.

The MC does not include any beamline-induced background effects, neither from particles that are exactly in-time (from the same parent 16 GeV pion hitting the target) nor from secondaries from another pion in a nearby 19 ns slot in the Fermilab Main Injector 53 MHz accelerator structure. Because activity is saved from 16 μs around each trigger, and because some incident particles should spatially leave much of the detector quiet, the data contain a record of the average beam-induced background around valid triggers.

The particle selection technique was developed and validated using the web-based MINERvA event display [11], in many cases with the help of undergraduate research assistants. The main selection requires the particle to appear in the detector at a location and time predicted by the measurement in the beamline. Events with substantial unrelated activity, especially if it is track-like, are rejected. There is about a 10% background mainly from muons, but also lower energy particles entering the detector with

the triggered event. Events with additional reconstructed activity within 250 ns before and 500 ns after are also removed. These selections reduce beam-induced backgrounds and also eliminate triggered particles that scattered substantially in the beamline before reaching the detector. The selections to reduce these unwanted events are applied to both the data and MC samples. Finally, we estimate and make a statistical subtraction of the remaining background and evaluate an uncertainty specific to each analysis.

The basis of the simulation uses Geant4 version 9.4p2 [13,14] and our best description of the detector geometry and material [1]. A summary of the material properties of each of the three detector regions is given in Table 1. The scintillator plane is made of 1.801 g/cm^2 of plastic scintillator, WLS fiber, and a co-extruded TiO_2 reflective coating. Added to this is another 0.226 g/cm^2 of epoxy and Lexan. The scintillator planes were made at the same facilities immediately following the production of MINERvA planes, and the modifications for assembling smaller planes make negligible difference. The uncertainty on the amount of the material in the assembled scintillator planes is the same 1.5% as for the MINERvA detector. In the ECAL portion of the detector there are planes of lead with thickness 2.30 g/cm^2 and in the HCAL version there is 20.4 g/cm^2 material that is 99%Fe and 1%Mn. The lead and iron absorbers are similar to those in the MINERvA detector, but we use the as-measured test beam detector quantities in the simulation and to evaluate material assay uncertainties (coincidentally) of 1.2% for each kind of absorber. The uniform,

simulated air gap from one plane to the next is an approximation to the as-measured air gap, and the absorbers are approximately in the middle of this air gap, in front of the associated scintillator plane. The air gaps and also the approximate nuclear interaction and radiation lengths are summarized in Table 1.

Almost all aspects of the detector response are simulated using details constrained by calibration data and bench tests, including Birks' law parameter measured from these data, described next in Section 5. The temperature correction is made to the data but not simulated. Crosstalk arises because each scintillator strip's light is directed onto a pixel in a 64 channel PMT, leading to optical and some electronic crosstalk, which is simulated and tuned to data. A few features are not simulated, of which PMT after-pulsing and PMT nonlinearity are the only significant ones, and only affect high pulse-height activity.

Proton range and proton single-particle energy resolution obtained with the MC give good description of the data, confirming that the beamline characteristics are well simulated. To study this, the sample of protons in the TE configuration is divided according to which was the furthest downstream plane with activity. The distribution of measured proton kinetic energy for protons that make it to plane 14 (an X plane) is shown in the left plot of Fig. 5. The distribution has a peak near 200 MeV corresponding to protons that were really at the end of their range, and a high energy tail from protons that experienced an interaction. The protons that are actually at the end of their range form a Gaussian-like peaked distribution which can be fit to obtain a mean energy and a resolution. This same sample is used later to select stopping protons for Birks' parameter measurement in Section 5, and potentially trackable protons for Section 11. The procedure is done separately for both data and simulated events; in neither case does selecting the subset of stopping protons involve a prediction of the range.

The proton range is well modeled by the simulation. The simulated protons stop 1.1% earlier than the data, which is a smaller discrepancy than the 1% beamline momentum plus 1.5% material assay uncertainties. A comparison of the Gaussian fit mean from the end-of-range peak is shown in the right plot of Fig. 5 for data and MC. Stopping protons are such a high resolution sample, the widths of those Gaussian fits (10–15 MeV, not shown) are primarily driven by the beamline and multiple scattering resolutions, not effects of the test beam detector, and are also accurately described by the simulation.

5. Birks' law parameter

Birks' law describes the quenching effect on scintillation photons produced by high, localized energy deposits. After calibration of the beam and detector, we measure Birks' law

parameter [7,8] for the MINERvA polystyrene scintillator [1]. Birks' law quenching is an important effect at the end of proton tracks and affects calorimetry measurements in the MINERvA and test beam detectors. A large sample of proton energy deposits at the end of their range is obtained using the selection described at the end of Section 4. We use the subset of events that appear to stop in planes 9–19 of the TE configuration and are in the peak of the distributions illustrated in Fig. 5.

Birks' empirical parameterization of the quenching factor to be applied to photons/MeV is

$$\text{Suppression factor} = \frac{1.0}{1.0 + \text{Birks parameter} \times (dE/dx)}$$

with one parameter, often abbreviated k_B with units of mm/MeV. This suppression is implemented in the MC and applied to MC deposits based on the ΔE and Δx as the simulation steps the particle through the active scintillator material. If the parameter k_B is too high, the MC will show a discrepancy of too much suppression in the energy per plane that increases toward the end of a proton's range, with the data having the higher energy response. The left plot in Fig. 6 shows such a trend using the default value of 0.133 ± 0.040 mm/MeV used by MINERvA until the present measurement. The mean energy loss is better described by the top MC line with lower parameter value and higher response as a function of the distance from the observed end of the proton's path into the detector.

The left plot of Fig. 6, and the extraction of a better value for Birks' parameter, is formed using the binned distributions of the energy deposited per plane. Two examples of the underlying data are shown on the right. The top one is for the third plane from the end, and one for the plane at the end (zero planes from the end). The plane at the end is the most sensitive to Birks' parameter, but does not have a Gaussian shape, requiring a more complex fitting technique than simply fitting the mean of the energy per plane. These plots are used here to describe how the fit is constructed from the binned data for each plane. In the two distributions on the right, the two MC lines shown in each plot are for the smaller uncertainty 0.0905 ± 0.015 mm/MeV at best fit.

Birks' parameter is extracted iteratively. The original default value of the parameter and its uncertainty are used to make three full MC samples to extract a new parameter and smaller uncertainty. As shown in Fig. 6, the MC samples with $\pm 1\sigma$ around the default value of k_B usually bracket the data. For a trial Birks' parameter, the predicted binned distribution is formed by interpolating between these two samples, or when necessary extrapolating slightly beyond these samples. By scanning through a full range of parameters, the one that returns the lowest χ^2 is used to seed the next iteration of the analysis.
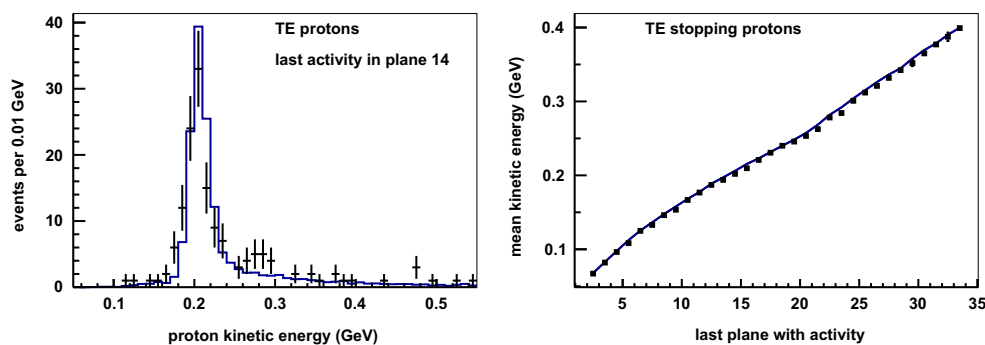

Fig. 5. The left plot is the kinetic energy distribution for protons that stopped in plane 14 in the TE configuration. Protons at the end of their range form a peak at 200 MeV. The right plot is the energy from the mean of a Gaussian fit to the peak for protons that appear to stop in each TE plane for data and MC. The MC protons stop 1.1% earlier than the data, a discrepancy which is smaller than the beamline momentum and material assay uncertainties. Most error bars are less than 1% and are too small to see.
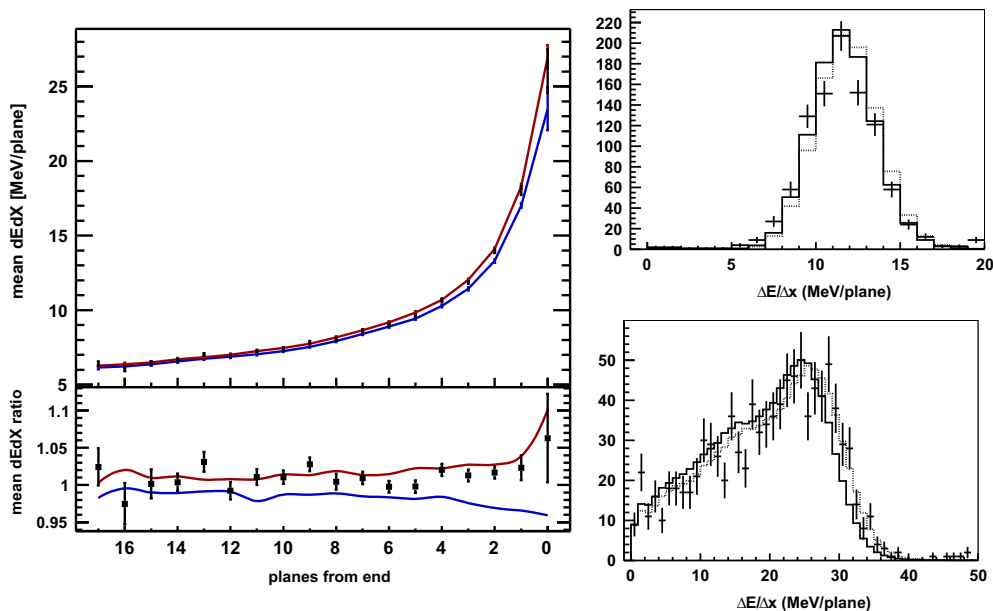
Fig. 6. The left plot shows the measured energy deposit per plane for data compared to the simulation with the before-fit Birks' parameter of 0.133 mm/MeV and the original −30% (top line) and +30% (bottom line) uncertainty on this parameter's initial value. The figures on the right show the underlying binned energy per plane, *at best fit* for the non-Gaussian end plane zero (lower right), and the more Gaussian plane third from the end (upper right). The MC distributions on the right show the smaller 17% uncertainty bounds, one shifted to higher values on the horizontal axis, one shifted lower, such that the best fit parameter (not shown) would lie between them in every bin, see discussion.

Not all available bins or planes are used in the fit. Planes further from the plane in which the proton stopped than the first fourteen are excluded from the analysis. They have low statistics because protons which only go nine planes into the detector do not contribute. To support systematic uncertainty studies, the analysis keeps only bins in the central region of each distribution in the right plots in Fig. 6. This ensures all bins in the fit will remain populated when systematically shifted samples are constructed. In the example of plane three, bins from 6.0 to 15.0 MeV are included, while plane zero includes bins from 10.0 to 32.0 MeV. In total, there are 123 bins across the fourteen planes-from-end included in the analysis.

The overall energy scale is an unconstrained parameter in the fit, which simultaneously accounts for both the uncertainty in the energy scale and the correlation between the calibrated energy scale and Birks' parameter. Every iteration of the fit scans over this parameter by applying a scale factor to each energy deposit of each MC event and reforming each histogram. The scale factor causes individual entries in the plots on the right side of Fig. 6 to shift higher or lower along the horizontal axis. This is equivalent to moving the mean of each distribution by the same amount, and allows the fit to seek a better χ^2 minimum.

Also, an amount of additional fluctuations of the simulated reconstructed energy is allowed to vary from strip to strip. This accounts for calibration effects beyond those that are explicitly in the simulation or removed from the data using calibrations. At best fit, the analysis yields the same additional 5.5% smearing as found for the MINERvA detector. This parameter was not changed for every iteration of the other parameters, only for values near the best fit result in the later iterations.

In summary, the best fit value is obtained using a parameter scan in this three-parameter space of Birks' parameter, energy scale, and smearing of reconstructed energy deposits. The procedure is iterated with a new MC built from the new parameter value and smaller ± shifted values. After three iterations the procedure reliably converges to the final result.

The best value for Birks' parameter is 0.0905 ± 0.015 mm/MeV. This value is near the -1σ limit of the original estimate used by MINERvA for analyses through 2014, confirming that we used

suitable Birks' effect uncertainties in prior publications. Future simulations using the new value have half the prior uncertainty. The best fit describes the data well, yielding a χ^2 of 124 for 120 degrees of freedom. In addition to showing the method of the fit, the two right figures in Fig. 6 show examples of the goodness-of-fit.

The measurement of Birks' parameter is dominated by systematic uncertainties. One of the largest is from the correlation with the energy scale, which is treated as an unconstrained parameter in the fit. The fit value is sensitive to variations of which protons, which physical planes, and which bins are included in the fit. Uncertainties in the material assay are propagated to the result using modified full MC samples. Extra smearing of the scintillator and PMT response to single energy deposits in the MC has a small effect. Two special sources of uncertainty, the effect of Geant4 step size and of PMT nonlinearity, are described below. All these effects are summarized in Table 2.

Birks' parameter is an effective parameter because it is obtained by matching MC to data. In addition to describing the quenching of scintillation light, it is accounting for the accuracy of the Geant4 energy loss simulation and our choice to use the default (adaptive) Geant4 step size. Allowing Geant4 to take more coarse steps, up to one scintillator bar per step, yields an increase in the simulated response of about 4% in the last plane and a slightly better $\chi^2 = 118$. The typical simulated Δx has increased, so $\Delta E/\Delta x$ has decreased, so there is less Birks' suppression applied. This large variation would cause a bias in the fit Birks' parameter of 9%, about half the total uncertainty. However, this particular measurement is specifically matched to the settings for Geant4 that are used by the MINERvA simulation as of late 2014. This uncertainty should be included when comparing to other measurements but is not an uncertainty on the resulting simulation used for MINERvA neutrino analysis.

The PMTs have a nonlinear response due to saturation effects that increase with dynode current and therefore total charge, an effect separate from the ADC to charge calibration. Nonlinearity has systematic effects on calorimetry and on Birks' parameter because it is unsimulated and uncorrected. This nonlinearity sets in for high instantaneous current at the anode, and so is a function of charge measured by the front end board's digitization circuitry.

Table 2
Percent systematic uncertainties on the value for Birks' parameter from different sources.

Source	Uncertainty
Uncertainty from fit	− 7%, + 5%
Proton selection	− 11%, + 3%
Geant4 step size	− 0%, + 9%
PMT nonlinearity	− 3%, + 0%
Material assay	± 5%
Physical planes	± 5%
MC energy smearing	± 3%
Choice of bins	− 3%, + 0%
Total	+ 16%, − 13%

The result is a suppression: the response in the data will be systematically lower than the equivalent MC events. MINERvA does not have a measurement under circumstances that are the same as the light propagating in our scintillator bars and WLS fiber. Instead, we have a reference nonlinearity curve informed by bench tests in which the suppression is parameterized by a quadratic function of the integrated current.

Because some light reflects from the mirrored far end of the WLS fiber and reaches the PMT at a later time, our ab initio upper bound on the amount of suppression is taken to be half the reference amount; this is the baseline uncertainty. The ΔE/plane profile in Fig. 6 is distorted by nonlinearity in different ways from either Birks' parameter or energy scale, enabling an in situ investigation of the size of possible nonlinearity. Applying nonlinearity that is 20% of the way from zero to the reference for every simulated digitized charge degrades the χ^2 by one unit, with a correlated shift in Birks' parameter. Thus at 25 MeV per plane (rightmost point in Fig. 6) we do not have sensitivity to nonlinearity effects with these data. The 20% constraint is used to add a component to the uncertainty for Birks' parameter measurement. Because this constraint is correlated with other aspects of this specific fit, the full upper bound of half the reference suppression is kept as the uncertainty for all calorimetry analyses.

Birks' measurement is consistent with other values for Birks' quenching parameter. The parameter value is expected to depend primarily on material formulation. A recent review of the properties of many materials including polystyrene is available in [15] with references and one additional later measurement [16]. These measurements are focused on heavily ionizing nuclear fragments and alpha particles which are important in dark matter and double beta decay experiments as well as nuclear fission studies. The technique is conceptually similar to using the end of a proton track but potentially more sensitive due to the enhanced ionization and granularity of the data. The analysis of [15] obtains a value of 0.0090 g/cm^2 MeV (with no uncertainty given) for polystyrene based scintillator. Using the 1.06 g/cm^3 density of polystyrene quoted in that analysis, this converts to 0.085 mm/MeV. This value and Birks' parameter result above for our scintillator formulation and density of 1.043 g/cm^3 are nearly identical.

6. Proton calorimetry

This test beam experiment is designed to constrain the uncertainty on the single particle calorimetric response to protons and pions. For low-multiplicity neutrino events we reconstruct the hadron response particle-by-particle using range, calorimetry, or a combination of the two. For high-multiplicity hadron systems from neutrino events, the total energy of the hadronic recoil system (everything but the outgoing charged lepton) is calorimetrically reconstructed. When the hadron(s) interact in the detector,

energy is spent unbinding nucleons from nuclei and other energy goes to neutral particles. An estimate of this missing energy is used to correct the observed response and obtain an unbiased estimator for the hadron system. In all cases, a major ingredient is the MC prediction for the single particle response, the observed energy in the detector for a given true energy, which is constrained with these data.

The hadron event is reconstructed by summing the calibrated energy measured in the scintillator. The standard tracking algorithm is applied to each event. If a track segment is found, the 3D location of hits on the track are known and used to make a correction for attenuation in the scintillator strip to the point where the particle passed. For all hits not on tracks, the attenuation estimate is made to the center of the strip. Then a correction for the passive material fraction for each plane is applied; a factor of 1.3 in the tracker, 2.1 in the ECAL, and 10.7 in the HCAL. Crosstalk is not included when the muon equivalent technique is used to set the energy scale, but is measured as a byproduct of that calibration. Because crosstalk is proportional to the total of the energy deposits, the measured crosstalk fraction of 4.2% is subtracted from both data and MC.

The activity recorded over the 150 ns integration time [12] is summed into the response, unlike the typical MINERvA neutrino analysis which uses a window from − 20 ns to + 35 ns around the peak in the cluster timing distribution. Activity later than 150 ns, from low energy neutrons and decay electrons, is not included. The latter is predicted to amount to a few percent of the available energy and appears in the detector over several microseconds.

For the proton calorimetry analysis, the beamline-induced backgrounds are reduced using additional selections. For the lowest proton energies, below 0.15 GeV for TE and 0.2 GeV for EH, the back half of the detector is not included calorimetrically at all and is used as a muon/pion veto by rejecting events with greater than 10 MeV of activity. Up to 0.3 GeV (TE) or 0.7 GeV (EH), backgrounds are reduced by using a 2 MeV threshold for activity in the last four planes to veto background activity from the beam. At the highest energies, there is no background rejection.

The resulting corrected estimate for the energy is compared to the available energy, which is just the kinetic energy for the proton. The distribution of this fractional response is the primary measurement and is calculated event-by-event. Then the events are binned by incident particle energy, and we compute the mean and RMS for each bin. The results for the mean are plotted in Fig. 7. The error band on the MC represents the total systematic uncertainty.

The proton response has several features in this energy range. At low energy, the probability for a proton nuclear interaction is low. As a result, there is little missing energy, and also the distribution of response is approximately Gaussian around its mean. At 0.3 GeV, the protons begin to enter the HCAL in the EH detector and begin to produce Δ resonances when they interact in nuclei in both EH and TE configurations. Both lead to a drop in response, the former as the high dE/dx end of a proton often happens in the steel, the latter because Δ production generically leads to lower response through neutral final states and energy lost to unbinding of additional nucleons.

The MC tracks the proton response well over the entire range. The ratio data/MC for the mean response in each energy bin is shown in Fig. 7. The MC has negligible statistical uncertainty; the systematic uncertainty on this ratio is shown as a band on the MC. and described in detail in Section 7. The data is shown with statistical uncertainties. Despite a cut on time-of-flight applied to data and MC, there may be additional pion background at 0.15 GeV in the proton data because those protons take 19 ns to travel the beamline. These data points, and the data point at 0.9 GeV, stand out in Fig. 7. They correspond to no other special features of the experimental setup, and have the character of fluctuations.
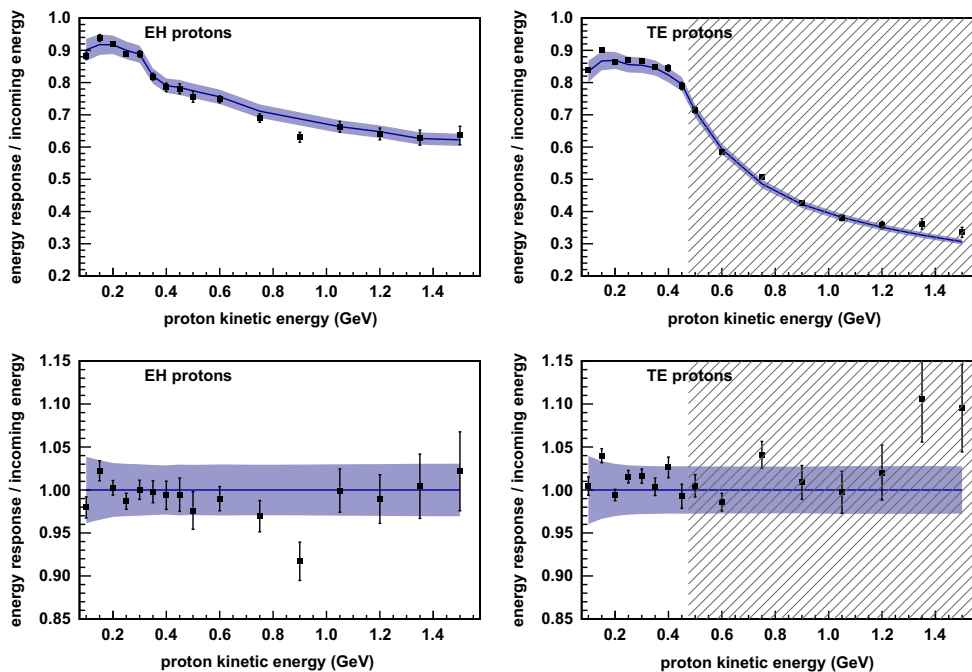
Fig. 7. Proton response for EH (left) and TE (right). The data points have statistical uncertainties, the MC line has an error band with the systematic uncertainties described in Section 7. The bottom plots show the ratio data/MC. The hatched TE region indicates energies where containment is so degraded that the measurement is not calorimetric.

The response at low energy for the TE detector is partly correlated to the tuning of Birks' parameter, because up to 0.25 GeV the two analyses use the same proton events. However, the strip response energy scale does not come from the free parameter in Birks' analysis, which would make this correlation even greater. Instead, the muon equivalent unit calibration was redone using the measured Birks' parameter to obtain the final strip energy calibration. Thus energy response offsets are correlated with Birks' parameter through its uncertainties, and less with the overlap of the data events.

At higher energies for the TE configuration, hatched in Fig. 7, there is a loss of containment of charged particles produced in the hadronic interaction. The calorimetric response no longer represents the kind of result we expect for the larger MINERvA detector. Instead, these points demonstrate that only the MC is still doing an adequate job describing the data.

In addition to the average response, it is important for MINERvA neutrino analyses that event-by-event fluctuations in the response are well simulated. Many neutrino distributions are strongly peaked in reconstructed energy or some other kinematic quantity, and an error in resolution will flatten or sharpen the MC peak relative to the data, causing a bias in unfolded distributions and fit parameters. The basic shape of the distribution of response particle-by-particle is well described, so it is adequate to use the RMS of the distribution to quantify the trend and the agreement, as shown in Fig. 8. Only statistical uncertainties on the RMS are shown, and no systematic uncertainty is quantitatively considered.

At all energies, the MC response has a lower RMS, and more so at low energy. The deviation can be taken to be a conservative uncertainty on the calorimetric resolution. A possible explanation for the degraded resolution in data is the addition of beamline induced backgrounds which are not simulated. Such backgrounds are not expected to have the same magnitude effect for higher energy protons, the pion sample, or the same origin as events in the MINERvA detector.

The resolution at 0.5 GeV is worse than at 0.3 GeV because of two effects mentioned previously. This is the region where proton interactions start to produce Δ resonances, which are also responsible for the decrease in response seen in the upper left plot of Fig. 7. Secondly, in the EH configuration, this is the energy range where protons start to reach the HCAL, and the high dE/dx endpoint of the proton is likely in the iron.

Of special interest is the resolution for the lowest energy protons which are contained in the tracker portion of the TE detector configuration. Such low energy protons are typically found at the vertex of a neutrino interaction from quasielastic and resonance production and include products of the intranuclear rescattering process. In the 0.05–0.2 GeV range, the resolution is around 17% and the distribution is nearly Gaussian. These protons are energetic enough to travel through more than one plane but not energetic enough to excite Δ resonances in the nucleus. The largest contributions to the resolution are from fluctuations at the end of the proton's range and (for data only) from beam-induced background activity. Above this energy, Δ production becomes important, reducing the fraction of protons that stop at the end of their range to about half the total. Also above 0.2 GeV, the distribution from which the RMS is computed picks up a low-side tail whose shape is well modeled by the MC.

7. Systematic uncertainties for single particle response

The systematic uncertainties on the single particle response described in this section also apply to the pion and electron measurements with only minor differences. It is convenient to present the systematic uncertainties together. This completes the discussion of the proton measurements, while providing information which is helpful for interpreting the pion measurements in Section 8. The significant sources of uncertainty are described in Table 3.

7.1. Beam momentum

This uncertainty is intrinsic to the design of the beam and the estimate of the momentum of the incoming particle. An uncertainty here has the effect of shifting the denominator of the
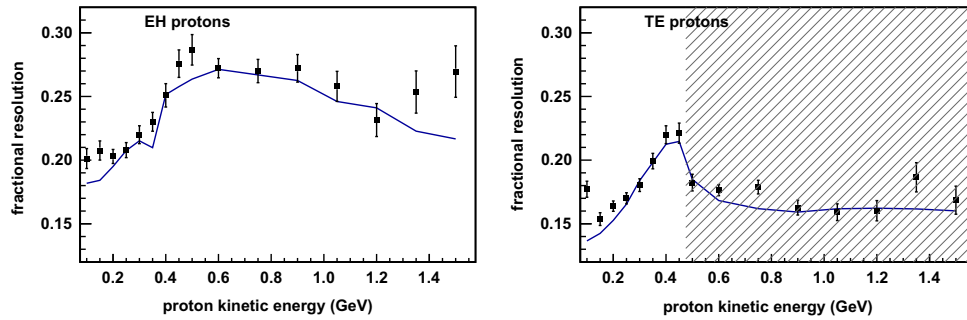
Fig. 8. Fractional resolution, from the RMS of the proton calorimetric response for the EH configuration (left) and TE (right). Only statistical uncertainties are shown on the data points, no uncertainties for the MC line. The hatched TE region indicates energies where containment is so degraded that the measurement is not calorimetric.

Table 3
Percent systematic uncertainties on the single particle fractional response for comparisons of the MC to data. Additional uncertainties on the energy scale and absorber material apply 2.0% equally to data and MC absolute response. The total range represents the evolution with energy from 0.1 to 0.4 GeV for TE protons, 0.1–1.0 GeV for EH protons, and 0.4–2.0 GeV for both pion samples. The statistical uncertainties for proton and pion response are shown in the figure for each data point, and are explicitly given in the table for both electron samples.

Source	TE p	EH p	EH π^+	EH π^-	EH e	TE e
Beam momentum	1.9%	1.9%	1.0–2.0%	1.0–2.0%	1.0	1.0
Beamline mass model	0.7	0.7	< 0.2	< 0.2	< 0.2	< 0.2
Birks' parameter	2.0–0.9	2.0–1.2	1.0	1.0	0.3	0.3
Correlated late activity	0.3	0.6	1.4	1.4	< 0.2	< 0.2
Temperature stability	1.0	1.0	1.0	1.0	1.0	1.0
Relative energy scale	0.6	0.6	0.6	0.6	0.6	0.6
PMT nonlinearity	0.7	0.7	0.9	0.9	0.4	0.2
Event selection	< 0.2	< 0.2	0.7	1.5	1.1	1.1
Crosstalk	0.7	0.9	0.5	0.5	0.5	0.5
Statistical	~1.0	~1.0	~1.0	~1.0	1.7	1.1
Total	3.3–2.7%	3.4–2.9%	2.6–3.4%	2.9–3.6%	2.6%	2.3%

fractional response. The uncertainty in the incident particle momentum is derived from the wire chamber survey and the measurement and simulation of the magnetic field. Because it is an uncertainty on the momentum, it translates differently to uncertainties on the available particle energy for protons and pions. The lowest energy protons pick up an additional 0.7% uncertainty due to the energy loss in the material of the beamline because they have higher ionization losses and those losses are a larger fraction of the total. With this and all other uncertainties, any energy dependence is included in the error bands in Figs. 7 and 9 and the total even if not summarized in individual lines in Table 3.

7.2. Birks' parameter

Even after producing a best fit Birks' parameter in Section 5, the remaining improved uncertainty is still one of the largest contributions to the accuracy of the result. Because low energy protons almost always have a high dE/dx activity at the very end of the proton's range, and because that activity is a larger fraction of the total energy for low energy protons, that sample is most affected by this uncertainty. The uncertainty in Birks' parameter is treated as uncorrelated with the energy scale and nonlinearity uncertainties.

7.3. Correlated late activity

Some uncertainties are revealed by varying event selection cuts. Proton response, and especially pion response, changes when a cut is applied to remove events when additional activity is reconstructed within 800 ns following the triggered event. The response in the MC, which has neither beamline-induced

backgrounds nor PMT afterpulsing simulated, is higher because of the correlation with neutrons from the hadronic interaction(s), electrons from π to μ to e decay, and other delayed activity. Activity beyond 150 ns from the trigger is not included in the calorimetric energy. However, neutron activity preferentially follow pions with low fractional energy response. The response for the data is the opposite; it falls slightly and ends about 1% below the MC prediction. Particles removed with this cut in the data due to late, unrelated beamline activity should be uncorrelated with the energy of the triggered event, and not bias the mean response. Instead, data particles with large shower activity and possibly less missing energy generate more afterpulsing and are more likely to have activity within the 800 ns after the event. If the effect was primarily afterpulsing, the default selection is optimal and this would not be a systematic uncertainty, but an investigation did not confirm that hypothesis. That the MC and data disagree on how the response changes could be a Geant4 modeling effect, which is what the experiment is designed to measure. However, we have not ruled out an experimental effect, so this is included in the uncertainty.

7.4. Temperature stability

The response of the detector to cosmic ray muons for the data is calibrated against the measured temperature in the experimental hall as a function of time. This accounts for the change over the course of the day and from day to day during the run. A correction is then applied to energy deposits in the beam data, while the simulation has no temperature dependence. The uncertainty is estimated as the difference between the responses of the high and low temperature halves of the dataset, after the correction is applied.
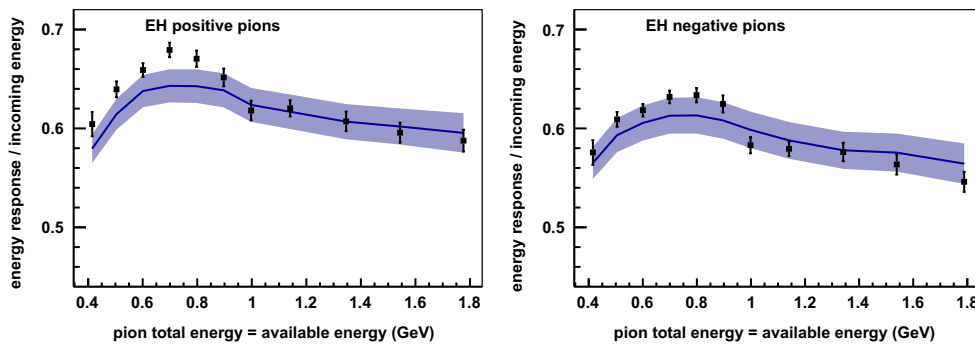
Fig. 9. Calorimetric response for positive (left) and negative (right) pions. The errors on the data are statistical only, while the error band on the MC represents the systematic uncertainties associated with comparisons between data and MC. A larger uncertainty of up to 4.2% (not shown) applies to the absolute response scale for both data and MC.

7.5. Relative energy scale

The calibration procedure uses a comparison of simulated cosmic ray muons to measured muons, so by construction the data/MC relative energy scale is well constrained. (The absolute energy scale is limited by our knowledge of the material model for the scintillator planes and affects both data and MC.) The only significant contribution to this relative uncertainty comes from observations of discrepancies between the TE and EH data sets. Within each subsample, there is no discernable time-dependent trend in the energy response that can be extrapolated between these two detector configurations. The uncertainty listed here is taken to be half the discrepancy seen in the muon calibrations between the TE and EH data sets.

7.6. PMT nonlinearity

A nonlinearity reference curve is available from bench tests of these photomultiplier tubes and is a suppression of response as a function of the total measured charge. Half the reference curve approximately accounts for the translation from bench test conditions to detector conditions with direct and reflected light. Birks' parameter measurement yields only an upper bound for the magnitude of this effect, but that result is obscured by correlations with other uncertainties. We use half the reference curve as the uncertainty here, applied to reduce the reconstructed energy of the MC on a strip-by-strip basis. Nonlinearity is a large effect for rare high activity strips, but for hadronic tracks and showers at these low energies the overall effect is modest. This effect is one way because there is no PMT nonlinearity in the simulation, so it serves only to move the simulated energy lower.

7.7. Event selection

For protons, variations in the event selection do not produce significant uncertainty, even near 0.15 GeV kinetic energy where the 19 ns pileup appears. There is an intrinsic electron and kaon background in the pion sample. Variations in those selections yield a 0.7% uncertainty for π^+ and twice the uncertainty for π^-.

7.8. Crosstalk

Optical and electronic crosstalk in the cosmic muon calibration gives an average contribution of $4.2 \pm 0.5\%$ to the energy in the detector, and the amount of crosstalk in the MC is tuned to reproduce this. Because the energy calibration of the detector specifically does not include crosstalk, the latter is subtracted from the total energy of each event. The remaining 0.5% contributes directly to the calorimetric uncertainty between data and MC.

Analysis of neutrino data also has crosstalk in the simulation tuned to the data, but uses multiple techniques depending on the analysis to deal with crosstalk, including thresholds, topological identification, and subtraction.

7.9. Absolute energy scale

There are additional effects which apply equally to both data and MC absolute energy scale and enhance the absolute uncertainty beyond the relative energy scale uncertainties. The most important comes from the material model for the scintillator planes and also the lead and iron absorber. They affect both the calibration of the energy deposits in the detector as well as how deep the hadronic activity propagates into the detector. They add an additional 2% in quadrature to the quantities in Table 3 and the vertical axis in the response figures for any situation where the absolute uncertainty is needed. The most important portion for calorimetry, from the calibration of the energy scale, yields an uncertainty on the calorimetric correction applied to both data and MC.

7.10. Geant4 step size

The simulation is affected by a number of different Geant4 settings, including some that are unrelated to the hadronic physics model. A setting of particular interest is the maximum step size allowed by the Geant4 adaptive step size algorithm. The baseline simulation uses essentially the default Geant4 settings, the same as used for the rest of the MINERvA experiment, so all the calibrations and measurements are done with a consistent set of parameters, and there is no uncertainty to assign. Purposely making the maximum step size 0.05 mm allows the adaptive algorithm to still choose smaller steps near material boundaries but never larger steps. This change results in a reduced MC response of 1% for pions and has no effect for 0.5 GeV/c electrons. The effect is consistent with causing an enhanced Birks' effect because then the simulation produces more highly quenched energy deposits; compare the opposite study in Section 5 of 4% enhancement in the last plane with activity for a more coarse stepping.

8. Pion calorimetry

Two separate samples of pions were obtained by running the beam magnets with different polarities. The EH π^+ sample was obtained concurrently with the proton sample while the π^- sample was from the data set taken the previous week. After these data were taken, the detector configuration was changed to

the TE configuration, but unlike for protons, containment in the TE is not adequate for a pion calorimetry measurement. Another difference is that the lowest beam momenta available cause the lowest pion energy for this analysis to be 0.35 GeV, just above the Δ production peak. The ECAL is less than one interaction length thick, but the HCAL is more than one interaction length. Very few pions stop at the end of their range in the detector, but many reach the HCAL before interacting.

The event selection and energy measurement proceed similar to the proton case, including correcting the observed energy for passive material, crosstalk, and the last-four-plane veto. The denominator for the fractional response for pions is taken to be the total energy; some of the pion mass energy will become reconstructed energy in the detector. For pions there is a potential background at low energy from electron contamination and at high energy from kaons (see Fig. 2) which is neither simulated nor subtracted. Variations in the selection process result in only small changes to the response.

The background due to unrelated activity from the beam has been estimated two ways. A measurement of activity 30 ns earlier than the triggered particle gives one estimate. For the lowest energy proton sample, another estimate is made by measuring activity beyond plane 30 where there should be negligible activity. When extrapolating these estimates to the whole detector and time of the event, they both yield the same 4 MeV per event on average. For the mean response, this is simply subtracted from the total energy before calculating the fractional response. At higher energy, the use of the last-four-plane veto leads to another downward bias of about 1% in the observed energy, estimated using the MC, because real hadron interactions put energy into those planes. This bias is removed with a MC-based energy dependent correction. The pion analysis procedure is different than the use of stricter cuts for protons but also leads to negligible uncertainty.

The MC describes the response to pions imperfectly, as shown in Fig. 9. The statistical uncertainty on the data is shown but is negligible for the MC. Systematic uncertainties (with their energy dependence) from Table 3 are incorporated into the MC error band. The MC models the single particle response to within 4% averaging the points up to 1.0 GeV, and 3% from there up to 2.0 GeV.

This level of agreement is adequate for MINERvA's neutrino program, is used to assess the single-particle hadronic response uncertainties for MINERvA analyses, and no correction factor is needed. However, the MC does not accurately model a change in behavior that starts at 0.9 GeV, where there is a mild inflection point in the MC predicted response. The onset and the magnitude of the discrepancy are the same for both π^+ and π^-, equivalent to a 5% decrease from low to high energy relative to the MC. The experimental systematic uncertainties permit some shape distortion for higher energy relative to low, about equally from the

beamline uncertainties, species selection, and beamline-induced backgrounds. When evaluated in quadrature, these could produce a $\pm 1.8\%$ relative change over this energy range, less than half what is observed. None of these systematic uncertainties would naturally produce a change over a short 0.2 GeV energy range near 0.9 GeV. If a future MINERvA neutrino analysis is sensitive to this, we will need to parameterize this effect instead of taking an overall uncertainty in the response.

In principle, these data are a test of not only just our ability to model the detector itself but also the ability to model the pion energy loss and reaction processes such as inelastic, absorption, charge exchange, and elastic scattering. We have investigated the sensitivity to model uncertainties using the Bertini cascade model [17] within Geant4, including consideration of pion cross-section data [18,19]. However, calorimetry is more sensitive to the total available energy than it is to differences in the types of outcomes for the first particle–nucleon interaction in the hadronic shower. Trial 30% modifications to the relative mix of outcomes have at most a 0.5% effect on calorimetry. Instead, increasing the probability of pions to interact (either elastically or inelastic with at least 10 MeV energy transfer) before reaching the HCAL enhances the response. By this definition of interaction, the mean free path in the ECAL is about 30 planes; lowering it by 20% (increasing the Geant4 pion nucleus cross-section) decreases the calorimetric response by 2%. An investigation of the trend reveals a correlation with the fraction of events that have negligible energy in the HCAL: the MC does not follow the data and underestimates this fraction starting at 0.9 GeV. Such an underestimate is also a predicted effect of a too-high mean free path, lowering it by 20% increases shifts this fraction up 2.5%. Differences between models in Geant4 and reality in principle could be energy dependent, so a tuned model could better describe the overall average response or separately the anomalous trend with energy.

The ratio of detector response to positive pions over detector response to negative pions cancels a number of common uncertainties and the trends described in the preceding paragraphs. The MC predicts that π^+ yields a 4.8% higher response than π^-. The measured ratio is 6.2%, with no energy dependence for either data or MC. The statistical uncertainty in the ratio in data is only 0.5% averaged over all energies. Another 0.6% uncertainty in the data/MC relative energy scale comes primarily from the unknown time or detector configuration dependent effect described in Section 7.5, which should conservatively be applied to interpret this ratio. There is no evidence for either an intensity effect (the π^+ data was at higher intensity), or an operational effect due to time or polarity in the beamline, nor a temperature effect. These uncertainties are judged by comparing two halves of each data configuration further split along these operational parameters, though these tests are themselves afflicted by 0.7% statistical uncertainty. This $6.2 - 4.8 = 1.4\%$ discrepancy is at two standard deviations, and it can
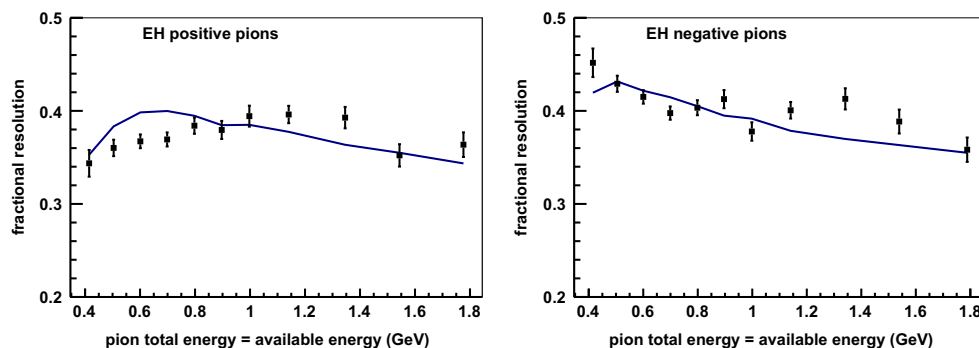

Fig. 10. Fractional resolution from the RMS of the calorimetric response for positive (left) and negative (right) pions. The statistical error on the RMS is shown for the data points. The predicted resolution from the MC is the line, and has no systematic uncertainties included.

be used as a conservative uncertainty on the ratio, when applying it to neutrino analyses.

As with the proton case, Fig. 10 shows the resolution on the pion fractional response. It is adequately modeled. Beam-induced backgrounds are a much smaller fraction of the total energy than for low energy protons, the Δ production peak is at an energy below the lowest energy data, and a large fraction of the events reach the HCAL, so there is none of the structure seen in the proton case.

9. Electron calorimetry

The electron samples are limited to energies in a range from 0.4 to 0.5 GeV but are useful for studies with the ECAL portion of the detector. The production of electrons is intrinsically lower in energy and fewer than pions and is predicted by an ab initio simulation of the beamline to be negligible for energies greater than 0.7 GeV. Furthermore, the TOF resolution prevents good identification of the few that are at higher energies. In the EH detector configuration, electrons in this energy range deposit 95% or more of their energy in the ECAL portion of the detector, and the response of the ECAL alone can be measured. The TE detector configuration is similar: the electron propagates through the tracker but does not shower extensively until the ECAL.

The electron sample is separated from the pion sample using a combination of topological and time-of-flight selections. Events that resemble late-interacting pions because they are tracked into the HCAL or because they have a substantial fraction of energy in the back half of the detector are rejected. Further, the number of strips recording activity is systematically more for electrons, and the variance in energy per plane for EM showers is much higher than for interacting pions. Using the MC, we estimate the efficiency for selecting electrons (pions) to be 61% (5%) for the TE and 73% (8%) for the EH configuration. The pion and electron peaks separate in time-of-flight by at least 0.7 ns at 0.5 GeV, easily separated given the 0.2 ns resolution of the TOF measurement. Extrapolating the pion distribution just above the TOF cut into the selected electron region in data yields an estimate of one pion background in 50 electron events. An eye-scan of the resulting events with the web-based MINERvA event display [11] yields one obvious background event which is removed, leaving 49 events total in the EH sample.

The resulting sample is analyzed similarly as previously described for protons and pions. The data for electrons and positrons for the EH configuration were combined into one sample; the MC is treated the same way. After correcting for passive material, crosstalk, and beamline-induced background activity, the response ratio is obtained for every event using the total electron energy as the denominator. The electron fractional response is found to be 0.763 ± 0.013 (statistical) in data and 0.740 ± 0.002 (statistical) in MC. There is an additional 2.0% relative systematic uncertainty between the data and MC, discussed in Table 3, bringing the total uncertainty to 2.6%. Further adding uncertainties from the material assay brings this to 3.3% absolute uncertainty. The data response is 3% higher than the MC predicts, a little more than the total relative uncertainty. The MC predicts a resolution of 11.5%, which is an adequate description of the low-statistics data.

The MC predicts that the response in the TE configuration is 3% higher than the EH configuration because most electrons ionize their way through the tracker before electromagnetic showers develop in the ECAL. The TE sample provides another 62 events, with more positrons than electrons because of the running conditions. Again a 3% discrepancy response is seen in these TE results, as with the EH results. The statistical uncertainty is smaller because of slightly better statistics and resolution. The data/MC relative total uncertainty is

2.3%, and the absolute uncertainty on the response is 3.0%. The MC prediction of a 9.1% resolution describes the data well.

The electron sample analyses are subject to the same uncertainties as the proton and pion results plus another 1.1% uncertainty due to the additional requirements to select electrons. Table 3 summarizes the uncertainties in the final two columns. Comparing the default MC to a variation with $\pm 1.2\%$ lead density in the ECAL reveals only a $\pm 0.15\%$ change in response for the TE configuration and $\pm 0.3\%$ change for the EH sample. Variations of the event selection contribute 1% uncertainty to the response. The absolute energy scale uncertainty is the same 2% and the data vs. MC relative uncertainty is 0.7% from the material model effects and calibrations described previously. Another 0.5% comes from the crosstalk model. Finally, the beam momentum uncertainty is 1% at these energies.

10. Calorimetry discussion

In addition to the extensive studies of high energy calorimetry described by Wigmans [20], there are several recent test beam measurements using scintillator and absorber sampling calorimeters and hadron simulations similar to MINERvA. Hadron calorimetry at energies below 2 GeV follows a process where one hadron typically undergoes two, one, or zero inelastic interactions, with a small number of outgoing charged particles. Unlike hadron calorimetry at higher energies, the processes are not easily characterized by the statistical $\sqrt{E}$ and $\sqrt{N}$ effects.

The MINOS neutrino experiment uses a detector made of scintillator and inch-thick iron, very similar to the MINERvA HCAL. Their test beam exposures in the CERN T7 and T11 beamlines [21] were analyzed to produce electron [22] and hadron [23] calorimetry results, among other measurements [24]. They compared their data to a GEANT3 simulation and found several discrepancies at the 3–6% level. However, our data are compared to a Geant4 simulation, so interpretation relative to the present analysis is indirect.

The CALICE experiment has data from operating several kinds of sampling calorimeters in beams at Fermilab and CERN. They use similar, Geant4 based hadronic and electromagnetic models, but their data is mostly at higher energy. The analysis of their data is ongoing. As of this writing, two publications [25,26] can be compared with the MINERvA test beam data.

Hadronic calorimetry is considered [25] for data taken with an iron-scintillator calorimeter. They find that Geant4 models underestimate the measured response by 3% at 8 GeV/c momentum, which is their lowest pion data available. This discrepancy is beyond the edge of their 2% uncertainty. The 8 GeV/c data is also the only one of the many model comparisons in their paper where Geant4 is using the same Bertini cascade model used in our simulation, shown in the lowest (blue) line in the lower left plot in their Fig. 6. Their data show a trend with energy such that the MC overestimates the data above 20 GeV or so, but remain consistent within their uncertainty estimates.

In the later paper [26], data from a tungsten segmented calorimeter is compared to Geant4 models for electrons, pions, and protons. The π^+ response for the same Bertini cascade model (but from Geant4 9.6.p2) describes their mean response very well from 3 to 8 GeV. The discrepancy is less than 2% while their uncertainty is around 3%. The comparisons in this later paper include the same models and some of the same energies as in [25], but using data from a different beam and an ECAL detector configuration. Agreement also follows for proton data in the same range. A similar result is obtained for positrons, agreement above 2 GeV. However, the simulation underestimates the data by 2.5% at 1 GeV, just within one standard deviation agreement for the lowest positron energy for which they have data.

Table 4
Summary of tracking efficiencies for the two configurations of the short-tracker combined with the same long-tracker algorithm.

Proton depth	Pion short tracker		Quasielastic short tracker	
	Data (%)	MC (%)	Data (%)	MC (%)
≥ 9 planes	$99.2^{+0.2}_{-0.3}$	99.8 ± 0.1	$99.5^{+0.2}_{-0.2}$	99.9 ± 0.1
8 planes	$96.2^{+1.2}_{-1.6}$	97.7 ± 0.6	$96.8^{+1.2}_{-1.6}$	98.3 ± 0.5
6 and 7 planes	$91.1^{+1.5}_{-1.6}$	96.5 ± 0.5	$93.5^{+1.3}_{-1.4}$	98.1 ± 0.4

Taken together, the MINERvA and CALICE data suggest that the Bertini cascade model from recent (9.4p2 and later) Geant4 does a good job of describing hadronic data at the 4% level in an iron-scintillator calorimeter through the combined range of energy. CALICE indicates that the electromagnetic cascade model applied to an ECAL style calorimeter also does very well. But the low energy data point that is similar to MINERvA's suggests that the MC underestimates the response in both cases.

11. Tracking efficiency

The proton sample in the TE detector configuration allows us to measure the proton tracking efficiency, defined as the probability that a proton will be reconstructed as a three-dimensional track object. The proton tracking efficiency, and that for pions, is important for measurements of neutrino differential cross-sections with specific proton and pion final states.

The sample is similar to the one used for Birks' parameter measurement where protons stop no later than plane 19, but without the requirement that its depth be consistent with a proton at the end of its range. Another difference is that the sample is extended to protons whose last activity is only as far as plane six. This analysis of tracking tests a combination of the standard MINERvA "long tracker" which requires a minimum of eleven planes in combination with either of two variations of the "short tracker" which can form tracks with as few as five planes of activity. For this analysis, the MC sample is four times the size of the data sample.

The efficiency for long tracks is nearly perfect. Specifically, the sample of protons with kinetic energy less than 0.4 GeV whose last energy deposit is between planes nine and nineteen (inclusive) are tracked with efficiency of $99.2^{+0.2}_{-0.3}\%$ in data and $99.8 \pm 0.1\%$ in MC. For the data, this corresponds to tracking 1520 out of 1533 protons in the sample. Around 60% of protons stop a distance consistent with the end of their range, and failing the tracking is highly correlated with a proton experiencing an interaction.

Differences between the MC and data begin to appear for samples of even shorter proton events. For the 185 protons that appear to stop in plane eight, 178 of them were tracked, which gives 96.2% compared to the MC 97.7%. For 338 protons that appear to stop in planes six and seven only 308 are tracked, 91.1% compared to the MC 96.5%. These subsamples have a 70% fraction with their stopping location at the end of their expected range. It is more likely in the data than the MC that the subset of events with a short proton event at the end of its expected range will not pass the tracking requirements.

The above results for protons were obtained with a short tracker configured for a neutrino pion production analysis [5]. A somewhat different configuration optimized for a quasielastic proton analysis [6] gives 1–2% higher efficiency, successfully tracking an additional 6, 1, and 8 events in the data subsamples for the shortest, 8-plane, and longest samples respectively, with a similar trend of better tracking in the MC. The efficiencies are summarized in Table 4.

The main reason for the difference between the two tracking techniques involves the choice of candidate clusters of activity to give to the tracking algorithm. The quasielastic proton algorithm is more permissive, allowing clusters with more hits and more energy that would be expected from a simply ionizing particle. The pion algorithm excludes these when deciding whether to form a track. In the case of very short, six-plane tracks, excluding one plane explains the difference between the two algorithms.

Overall, the results suggest that tracking efficiency is adequately modeled (within 1%) for tracks greater than 9 planes, which makes it a negligible uncertainty for neutrino analyses. In contrast, we can use a data-based correction of as much as 5% to the efficiency for shorter track lengths, relative to the MC predicted efficiency. In the MINERvA detector, there is activity near the neutrino interaction point and wider range of angles relative to the detector axis, which are not addressed by the test beam sample. Therefore, this efficiency correction should be on top of the MC prediction for efficiency that considers other effects seen in real neutrino interactions.

12. Conclusion

We have measured the performance of the tracking and calorimetry of the MINERvA detector by exposing a scaled-down version of the detector to a test beam of low momentum protons, pions, and electrons from the Fermilab Test Beam Facility. These data provide a constraint on Birks' law of saturation effect for our formulation of polystyrene based plastic scintillator. The calorimetric response to protons and pions within the range of energies tested yields uncertainties of 4% when the single particle calorimetric response is used in neutrino analyses. There are several effects that could be interpreted as two standard deviation fluctuations relative to the systematic uncertainties, but overall the MC describes the data and its resolutions well. The electron sample yields a similar uncertainty. Tracking performance is well modeled, and we have measured a small discrepancy between the performance of tracking in the data and simulation.

References

[1] L. Aliaga, et al., Nuclear Instruments and Methods in Physics Research Section A 743 (2014) 130. http://dx.doi.org/10.1016/j.nima.2013.12.053 arXiv:1305.5199.

[2] L. Fields, J. Chvojka, et al., Physics Review Letters 111 (2013) 022501, arXiv:1305.2234, http://dx.doi.org/10.1103/PhysRevLett.111.022501.

[3] G. Fiorentini, D. Schmitz, P. Rodriguez, et al., Physics Review Letters 111 (2013) 022502, arXiv:1305.2243, http://dx.doi.org/10.1103/PhysRevLett.111.022502.

[4] B. Tice, M. Datta, J. Mousseau, et al., Physics Review Letters 112 (2014) 231801. arXiv:1403.2103, http://dx.doi.org/10.1103/PhysRevLett.112.231801.

[5] B. Eberly, et al., Charged Pion Production in ν_μ Interactions on Hydrocarbon at $\langle E_\nu \rangle = 4.0$ GeV. arXiv:1406.6415.

[6] T. Walton, M. Betancourt, et al., Measurement of muon plus proton final states in ν_μ Interactions on Hydrocarbon at $\langle E_\nu \rangle = 4.2$ GeV. arXiv:1409.4497.

[7] J.B. Birks, Proceedings of the Physical Society Section A 64 (1951) 874.

[8] J.B. Birks, The Theory and Practice of Scintillation Counting.

[9] R. Burnstein, et al., Nuclear Instruments and Methods in Physics Research Section A 541 (2005) 516. http://dx.doi.org/10.1016/j.nima.2004.12.031 arXiv:hep-ex/0405034.

[10] R. Fruhwirth, Nuclear Instruments and Methods in Physics Research Section A 262 (1987) 444. http://dx.doi.org/10.1016/0168-9002(87)90887-4.

[11] N. Tagg, et al., Nuclear Instruments and Methods in Physics Research 676 (2012) 44. http://dx.doi.org/10.1016/j.nima.2012.01.059 arXiv:1111.5315.

[12] G. Perdue, et al., Nuclear Instruments and Methods in Physics Research Section A 694 (2012) 179. http://dx.doi.org/10.1016/j.nima.2012.08.024 arXiv:1209.1120.

[13] S. Agostinelli, et al., Nuclear Instruments and Methods in Physics Research Section A 506 (2003) 250. http://dx.doi.org/10.1016/S0168-9002(03)01368-8.

[14] J. Allison, K. Amako, J. Apostolakis, H. Araujo, P. Dubois, et al., IEEE Transactions on Nuclear Science NS-53 (2006) 270. http://dx.doi.org/10.1109/TNS.2006.869826.

[15] V. Tretyak, Astroparticle Physics 33 (2010) 40. http://dx.doi.org/10.1016/j.astropartphys.2009.11.002 arXiv:0911.3041.

[16] L. Reichhart, D.Y. Akimov, H. Araujo, E. Barnes, V. Belov, et al., Physical Review C 85 (2012) 065801. http://dx.doi.org/10.1103/PhysRevC.85.065801 arXiv:1111.2248.

[17] A. Heikkinen, N. Stepanov, J.P. Wellisch, Bertini intranuclear cascade implementation in GEANT4, eConf C0303241, 2003, MOMT008. arXiv:nucl-th/0306008.

[18] D. Ashery, I. Navon, G. Azuelos, H. Walter, H. Pfeiffer, et al., Physical Review C 23 (1981) 2173. http://dx.doi.org/10.1103/PhysRevC.23.2173.

[19] B. Allardyce, C. Batty, D. Baugh, E. Friedman, G. Heymann, et al., Nuclear Physics A 209 (1973) 1. http://dx.doi.org/10.1016/0375-9474(73)90049-3.

[20] R. Wigmans, International Series of Monographs on Physics 107 (2000) 1.

[21] P. Adamson, G. Crone, L. Jenner, R. Nichol, R. Saakian, et al., Nuclear Instruments and Methods in Physics Research Section A 556 (2006) 119. http://dx.doi.org/10.1016/j.nima.2005.10.072.

[22] P.L. Vahle, Electromagnetic Interactions in the MINOS Detectors (Ph.D. thesis), 2004.

[23] M.A. Kordosky, Hadronic Interactions in the MINOS Detectors (Ph.D. thesis), 2004.

[24] A. Cabrera, et al., Nuclear Instruments and Methods in Physics Research Section A 609 (2009) 106. http://dx.doi.org/10.1016/j.nima.2009.07.016 arXiv:0902.1116.

[25] C. Adloff, et al., Journal of Instrumentation 8 (2013) 07005. http://dx.doi.org/10.1088/1748-0221/8/07/P07005 arXiv:1306.3037.

[26] C. Adloff, J.J. Blaising, M. Chefdeville, C. Drancourt, R. Gaglione, et al., Journal of Instrumentation 9 (2014) P01004. http://dx.doi.org/10.1088/1748-0221/9/01/P01004 arXiv:1311.3505.